ADVANCING EARTH AND SPACE SCIENCES

JGR Earth Surface

RESEARCH ARTICLE
10.1029/2025JF008921

Seeing Through the Noise: Implications for Signal Preservation in Sediment Flux Time Series From Erosional Systems

L. O. Roberge[1], N. M. Gasparini[1], K. M. Straub[1], B. Campforts[2], and F. J. Pazzaglia[3]

[1]Department of Earth and Environmental Sciences, Tulane University, New Orleans, LA, USA, [2]Department of Earth Sciences, Vrije Universiteit Amsterdam, Amsterdam, The Netherlands, [3]Department of Earth and Environmental Sciences, Lehigh University, Bethlehem, PA, USA

Key Points:

- Sediment flux and landscape form are most unsteady when erosion rates from landslides and fluvial processes are most balanced
- Coupled hillslope-fluvial processes produce a tripartite sediment flux power spectrum that reveals timescales of external signal shredding
- Interactions between transport processes can generate emergent correlation timescales critical for sedimentary signal preservation

Supporting Information:

Supporting Information may be found in the online version of this article.

Correspondence to:

L. O. Roberge,
lroberge@tulane.edu

Citation:

Roberge, L. O., Gasparini, N. M., Straub, K. M., Campforts, B., & Pazzaglia, F. J. (2026). Seeing through the noise: Implications for signal preservation in sediment flux time series from erosional systems. *Journal of Geophysical Research: Earth Surface*, *131*, e2025JF008921. https://doi.org/10.1029/2025JF008921

Received 4 OCT 2025
Accepted 3 JUL 2026

Author Contributions:

Conceptualization: L. O. Roberge, N. M. Gasparini, F. J. Pazzaglia
Data curation: L. O. Roberge
Formal analysis: L. O. Roberge
Funding acquisition: N. M. Gasparini
Investigation: L. O. Roberge
Methodology: L. O. Roberge
Project administration: L. O. Roberge, N. M. Gasparini
Resources: N. M. Gasparini
Software: L. O. Roberge, B. Campforts

Abstract Allogenic forcing of sediment production generates sedimentary signals that we use to understand the past. These signals may be buffered or shredded by autogenic processes as they travel through sediment routing systems from source to sink. Studies on signal propagation tend to focus on either signal buffering by deterministic fluvial networks or signal shredding by stochastic processes. Stochastic processes generate noise that can obscure or degrade signals, especially below a threshold correlation timescale inherent to each process. It remains unclear whether this timescale exists when stochastically and deterministically modeled processes interact with each other. We address this knowledge gap by coupling stochastic landsliding and deterministic fluvial processes in a 2D numerical landscape evolution model in which we vary landslide frequency, sediment erodibility, and fluvial transport length scale to generate various dynamic steady state scenarios. We explore how the interaction of the landslide and fluvial processes affects landscape morphology and sediment export from the catchment. Though landslides produce instantaneous mass fluxes from hillslopes to channels, the deposited material can only be slowly evacuated by the fluvial system. This creates an emergent correlation timescale set by the residence time of landslide deposits. Efficient fluvial systems erode deposits faster and have shorter correlation timescales; therefore, they should be more likely to transmit higher-frequency signals down-system. These results can be used to predict where paleo-tectonic and paleo-climatic signals are more likely to be preserved in strata.

Plain Language Summary Mountain landscapes can be divided into hillslopes and rivers. Steep mountain hillslopes are shaped by landslides, which deliver dirt and rock (sediment) into mountain rivers. How quickly a river can erode a landslide sediment deposit depends on the size of the sediment and the regularity of flooding. In this study, we use a computer model to study the link between mountain hillslopes and rivers. We are motivated to understand under which conditions external events, such as periodic changes in climate, can produce a noticeable change in the sediment load of a river leaving a mountain range. We use our model to explore a range of scenarios, including differences in landslide frequency and sediment grain size. The landscape changes in predictable ways. When landslides are less frequent or produce smaller sediment grains, rivers dominate the landscape and efficiently transport away the sediment. On the other hand, frequent landslides that deliver larger sediment grains to the rivers lead to longer hillslopes and longer times for the river to evacuate sediment from the catchment. We find that longer evacuation times mean it is less likely that the sediment load leaving the mountain range will show a distinguishable signal from external events.

1. Introduction

Periodic allogenic (external) tectonic and climatic forcings can create signals, such as changes in sediment composition, size, or volumetric flux (Q_s, our focus in this study). Q_s signals produced in erosional catchments must travel through sediment routing systems before reaching sedimentary sinks where they may eventually become encoded as strata in the rock record. Along their journey down-system, Q_s signals may become buffered or shredded by autogenic (internal) processes that influence sediment transport, deposition, and remobilization. Buffering is the muting of a signal when the allogenic forcing acts over a timescale shorter than the landscape's response time (RT, the time a landscape takes to completely adjust to a new boundary condition) (Allen, 2008; Straub et al., 2020). Shredding occurs when autogenic stochastic processes distribute a signal across space and time such that it can no longer be reconstructed (Jerolmack & Paola, 2010; Straub et al., 2020). Understanding the

Supervision: N. M. Gasparini, K. M. Straub, B. Campforts, F. J. Pazzaglia
Validation: L. O. Roberge
Visualization: L. O. Roberge
Writing – original draft: L. O. Roberge, N. M. Gasparini
Writing – review & editing: N. M. Gasparini, K. M. Straub, B. Campforts, F. J. Pazzaglia

effects of autogenic processes on the erosion, transport, and deposition of sediment in erosional catchments is essential for interpreting paleo-tectonics and paleo-climate from stratigraphy.

Recent studies of signal propagation have fallen into two broad categories: those studying signal shredding by stochastic autogenic processes (e.g., Griffin et al., 2023; Jerolmack & Paola, 2010; Pizzuto et al., 2017), and those studying buffering by deterministic fluvial networks (e.g., Castelltort & Van Den Driessche, 2003; Godard et al., 2013; Li et al., 2018; Sharman et al., 2019). Using different modeling approaches, Jerolmack and Paola (2010), Pizzuto et al. (2017), and Griffin et al. (2023) show that although autogenic storage and release of sediment may shred short-term signals, long-term signals may remain partially preserved. Theory developed from field and laboratory measurements suggests that the transport of mass over the Earth's surface is noisy, but that over some timescales this noise has structure (Jerolmack & Paola, 2010). Short-term temporal correlation (red noise) can be distinguished from temporal independence (white noise) across moderate timescales and temporal anti-correlation (blue noise) at longer timescales, all caused by the internal dynamics of sediment transport processes (e.g., Ganti et al., 2024; Griffin et al., 2023). It is theorized that a key timescale exists (T_{RW}) that separates correlated (R, red) from uncorrelated (W, white) noise, below which propagating environmental signals get significantly degraded (Griffin et al., 2023). Li et al. (2018) explored the time lag (buffering) effect of a dendritic fluvial network on sediment flux (Q_s) signals using a detachment-limited stream power model in which no sediment storage is possible. Despite the lack of autogenic processes, the fluvial network did not produce a detectable signal for any rock uplift pulse shorter than 25% of the catchment's RT. With a similar model, Godard et al. (2013) found that the frequency of periodic precipitation forcing altered the amplitude of a Q_s signal at the outlet, with a specific period maximizing the signal strength. Notably, the buffering models do not consider the stochastic processes brought up by the shredding models and vice versa.

Here, we bring together the deterministic and stochastic approaches to explore how different processes interact to impact signal propagation and preservation. We couple stochastic landsliding with deterministic fluvial processes in a 2D numerical landscape evolution model (LEM) and explore the following questions: How do the stochastic fluxes of sediment from hillslopes interact with the buffering effects of a fluvial network to affect the transmission of volumetric sediment flux down-system? Does the coupled system have a characteristic shredding timescale consistent with the transition from correlated red to uncorrelated white noise T_{RW}? If so, what processes cause that noise transition and which model parameters govern the shredding processes? How do those model parameters affect the timescale T_{RW}?

2. Background

The work here builds on the concepts developed by others using numerical and physical avalanching sand and rice pile models (Frette et al., 1996; Griffin et al., 2023; Hwa & Kardar, 1992; Jerolmack & Paola, 2010). In these experiments, a steady feed of rice grains is added to the top of a pile, below which there is a weighing scale. As grains are added, the pile eventually oversteepens and an avalanche occurs, flowing down the pile to deposit on the scale. These simple systems produce stochastic sediment storage and release useful for understanding the often complicated sediment transport processes in field systems. However, they are not perfect analogs. For example, in comparison to fluvial systems in which fluid flow entrains and transports granular material, the rice grains begin to move only due to gravity and are not transported by another medium. Because of this, while a change in sediment supply can affect a river system's transport behavior (e.g., changes in slope and transport rate), the behavior of rice avalanches (e.g., size and duration) is independent of sediment supply (Griffin et al., 2023), Despite these limitations, avalanching rice piles can provide great insight into field systems and noise structure because they act across characteristic timescales.

Jerolmack and Paola (2010) and Griffin et al. (2023) show that the noise generated by dynamic steady state mass fluxes from stochastic rice pile avalanches is structured over certain timescales (Figure 1). Timescales shorter than the duration of a single failure event are characterized by correlation (or red noise) in mass flux as the avalanche deposits over time onto the scale. This correlation disappears at timescales longer than the longest failure event, where the red noise transitions to white (uncorrelated) noise. Marking the transition from red (R) to white (W) noise is the timescale T_{RW}. Power spectral analysis shows that propagating mass flux signals get significantly degraded at timescales below T_{RW} (Griffin et al., 2023). The uncorrelated white noise regime continues to another inflection point, past which anti-correlation (B, blue noise) takes over. This is the second key timescale, T_{WB}, which is caused by a finite size effect. This marks the time required for the system to re-fill after

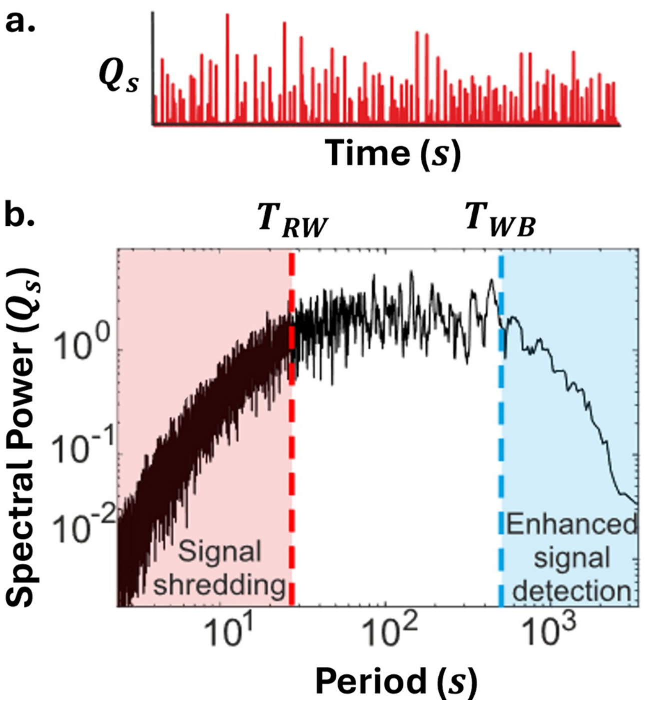

Figure 1. Diagram of a noisy sediment flux time series, Q_s, caused by storage and release of sediment (a) and its power spectrum (b). When transformed into a power spectrum, the noisy time series exhibits a clear tripartite structure characterized by increasing power over short timescales (red noise), constant power over moderate timescales (white noise), and decreasing power over long timescales (blue noise). The transition timescale between red and white noise, T_{RW}, marks the longest timescale below which input signals are shredded or degraded, while the transition timescale between white and blue noise, T_{WB}, marks the shortest timescale above which the signal-to-noise ratio decreases allowing for enhanced signal detection (adapted from Griffin et al., 2024).

very large avalanche events. The spectral power generated by the autogenic processes in the rice pile system reaches its maximum in the white noise regime between the two key timescales. Input mass flux signals are not degraded over the timescales between T_{RW} and T_{WB}, but the signal-to-noise ratio may be small, and the signal may therefore be difficult to detect (Griffin et al., 2023). The signal-to-noise ratio increases as spectral power decreases for timescales above T_{WB}, so long-period (low frequency) signals tend to be more easily detected (Griffin et al., 2023). Indeed, such long-period environmental and tectonic sedimentary signals have been quantified in stratigraphy (e.g., Mason et al., 2019; McNeill et al., 2019).

T_{RW} scales as a function of system size; a large rice pile can generate large avalanches that take a long time to flux out of the system, while the duration of avalanches generated by a small rice pile is inevitably shorter (Griffin et al., 2023). T_{WB} is also affected by system size, as larger failures take longer to re-fill. However, it is also a function of the input rate of rice grains; the faster the input rate, the faster the refilling process, and the shorter the timescale for T_{WB} (Griffin et al., 2023).

3. Experimental Methods

We use an LEM to explore how stochastic landsliding affects the morphology, dynamics, and sediment delivery of dynamic steady-state erosional catchments. The LEM is constructed using the Landlab modeling toolkit, an open-source Python environment for modeling planetary surface processes (Barnhart et al., 2020; Hobley et al., 2017). We couple four process components following the HyLands model configuration (Campforts et al., 2020, 2022): *SpaceLargeScaleEroder* to model fluvial incision, transport, and deposition (Shobe et al., 2017), *BedrockLandslider* to model stochastic landsliding (Campforts et al., 2020), *DepthDependentDiffuser* to model sediment transport by hillslope creep (Barnhart et al., 2019), and *ExponentialWeatherer* to model bedrock weathering and soil production (Barnhart et al., 2019). In every time step, the landscape is first uplifted, then bedrock is weathered (*ExponentialWeatherer*), that weathered material is transported downslope (*DepthDependentDiffuser*), then river channels erode and transport material downstream (*SpaceLargeScaleEroder*), and finally landslides occur (*BedrockLandslider*). A more detailed description of the numerical model setup is available in the Supporting Information S1.

The model landscape is a synthetic catchment subject to steady uplift for the duration of each model run. There is a single outlet through which sediment is transported out of the domain. The addition of stochastic landsliding to an otherwise deterministic model generates a dynamic landscape with complex interactions between geomorphic processes. Landslides occur instantaneously, but their deposits leave a lasting effect on the landscape. They cover valley bottoms with sediment that takes time to evacuate, causing temporary pauses to fluvial bedrock incision as the rivers erode the deposits. This elevates sediment flux for a period of time. Large enough deposits can last for thousands of years and cause knickpoints to develop or in some cases can redirect a river channel and cause lateral migration of the valley as the river erodes one side. Further, a large landslide deposit in the valley bottom locally increases the base level for the hillslopes, slowing hillslope erosion. The landscapes are in dynamic equilibrium for the entire duration of each model run, but at no point are they static. Like avalanching rice pile experiments (Griffin et al., 2023; Jerolmack & Paola, 2010), the internal dynamics generate noise in the output Q_S even though the input of material, in the form of uplifting bedrock, is steady.

We calculate several landscape metrics to describe the morphology of the catchment. We measure a time series of Q_s at the outlet of the catchment for the duration of a model run. We then apply the multi-taper method of spectral analysis to determine the time series power spectrum. We then analyze the structure of the spectrum to find transition timescales (e.g., T_{RW}) and relate them quantitatively to the processes governing sediment transport. We explore the effects of catchment size and variations in three model parameters: landslide return time (t_{LS}),

Table 1
Model Parameter Values Used in All Model Scenarios

Parameter name	Symbol	Units	Value
Cell size	dx	m	50
Timestep	dt	yr	50
Total model run time	t	yr	20,000,000
Rock uplift rate	U	mm yr^{-1}	1
Porosity of sediment layer	φ_{sed}	–	0
Erodibility of bedrock	K_r	m^{-1}	0.00001
Area scaling exponent	m	–	0.5
Slope scaling exponent	n	–	1
Initial soil depth	H_{init}	m	0
Angle of internal friction	φ	degrees	35
Hillslope diffusion efficiency constant	k	m yr^{-1}	0.1
Hillslope transport decay depth	H^*	m	0.1
Maximum soil production rate	P_0	m yr^{-1}	0.0003
Soil production depth-decay constant	P^*	m	0.44

erodibility (K_s) of the landslide deposits, and the net effective settling velocity parameter (V) of fluvially entrained sediment. Time series analysis begins after the synthetic landscape has reached a dynamic equilibrium. Thus, the results describe only the dynamic steady state behavior of the system. A more detailed description of these methods and experiments follows.

3.1. Model Domain and Scenarios

We first generate a base case model scenario. We then complete a suite of experiments to compare with this base case. These experiments systematically vary catchment drainage area, landslide return time (t_{LS}), landslide deposit erodibility (K_s), and net effective settling velocity parameter (V) of fluvially entrained sediment. The base scenario domain is composed of a synthetic 5 km long by 5 km wide grid of square cells with a spatial resolution of 50 m. The initial grid is seeded with randomly generated microtopography and allows drainage out of a single outlet point in the south-west corner. The temporal resolution is 10 years, and the total run time is 20 million years of dynamic steady state, which begins after the initial model spin-up time in which the landscape adapts to the initial conditions.

Table 1 shows the values of all model parameters for the base scenario. These are based on measured values from the Pagliara watershed in northeastern Sicily, Italy (Pavano et al., 2016, 2024). The Pagliara is a rapidly uplifting mountainous catchment that is a good example of a source-to-sink sediment routing system with a relatively short transport zone (main channel length: 12 km) through which sedimentary signals can travel quickly. Additionally, it is susceptible to landslides and is of a small enough size to be amenable to relatively high-resolution landscape evolution modeling (catchment area: 27 km^2). We use this real-world catchment as a guideline to ensure that the base scenario reproduces realistic topography and erosion rates. There is no intention of replicating the exact morphology of the Pagliara watershed or simulating its tectonic history; the model represents a generic catchment that could conceivably occur on Earth in the present day.

Note that V is not the still-water particle settling velocity (see Davy & Lague, 2009; Shobe et al., 2017). It should be thought of as a model parameter that governs the transport length scale of entrained sediment; low values for V cause fluvially entrained material to remain longer in suspension and travel further downstream compared to high V values, which cause sediment to more quickly drop out of suspension and re-deposit onto the channel bed.

Note also that the landslide return time parameter, t_{LS}, does not represent the exact return time of each landslide. Landslides are initiated at "unstable" grid nodes where the topographic slope exceeds the angle of internal friction. Whether a landslide occurs at an "unstable" node during a given timestep depends on the node's probability of landsliding and a stochastic sampling scheme. The temporal probability of landsliding is driven by the landslide return time parameter, t_{LS}. This is the "model" return time, which controls how often individual critical nodes will translate into a landslide. However, since landslides are larger than individual cells, their effective return periods are not the same as t_{LS}.

For the base scenario, K_s is set to 10^{-4} m^{-1} and V is set to 1 m/y. Landslide return time, t_{LS}, is set to a value of 10^3 y in order to cause many landslides every 10-year timestep. We then set up 3 suites of model runs in which we vary V, K_s, and t_{LS}. Each suite is composed of 3 model runs: S, M, and L, in which the parameter is set to a "small," "moderate," or "large" value, respectively (Table 2). In suite 1, we adjust t_{LS} by two orders of magnitude for each run. In suite 2, we adjust K_s by a half order of magnitude for each run. In suite 3, we adjust V by one order of magnitude for each run. Note that the base scenario uses the "moderate" values for K_s and V but the "small" value for t_{LS}.

Finally, we re-run the entire series of models on catchments of different sizes to determine whether this influences sediment export. We use square catchments with sides of length 2, 3, 4, 5, and 10 km (varying drainage area between of 4 and 100 km^2) to test the effects of catchment size (Table 3).

All experiments use a constant rock uplift rate of 1 mm/yr. During the 20-million-year simulations, we output data every 50 years, resulting in 400,000 outputs for calculating time series and landscape metrics.

Table 2
Model Parameter Values Used in t_{LS}, K_s, and V Experiment Suites

			Value for model run		
Parameter name	Symbol	Units	S	M	L
Landslide return time	t_{LS}	yr	1×10^3 [a]	1×10^5	1×10^7
Erodibility of sediment	K_s	m^{-1}	5×10^{-5}	1×10^{-4}[a]	5×10^{-4}
Net effective settling velocity	V	m yr^{-1}	0.1	1 [a]	10

[a]When one parameter is varied, the other two are held to this base scenario value.

3.2. Landscape Metrics

The landscape metrics we use to describe catchment morphology are total relief, hillslope-channel threshold drainage area, hillslope gradient, and normalized channel steepness (k_{sn}). As mentioned above, even at a steady state, the modeled landscapes are dynamic, so the value of each metric changes through time. Each 20-million-year model run produces a distribution of 400,000 values (one every 50 years) for each landscape metric. We report the median and the median absolute deviation (MAD) of each distribution. These statistical measures are chosen because they are robust against outliers and long tails, which occur in some of the distributions.

Total relief (L) is the difference in the elevation between the highest and lowest points in the catchment. Since the base level is set to zero, total relief is equivalent to the elevation of the highest point in the landscape.

Hillslope-channel threshold drainage area (L^2) is calculated using the *pwlf* Python package to detect a breakpoint in the slope-area relationship in log-log space. Though more advanced methods exist for high-resolution topographic data (e.g., Clubb et al., 2014), breakpoint detection works well to distinguish hillslope and fluvial domains on synthetic landscapes (e.g., Campforts et al., 2022). The drainage area at that breakpoint represents the threshold at which geomorphic transport processes transition from hillslope-dominated to channel-dominated (e.g., Tucker & Bras, 1998).

Hillslope gradient for each output is calculated as the median value of the local gradient between all adjacent "hillslope" grid nodes. We characterize channel steepness using the normalized channel steepness index (k_{sn}) on "channel" grid nodes, calculated as $k_{sn} = SA^{m/n}$ (Wobus et al., 2006). Here, $m = 0.5$ and $n = 1$, so k_{sn} has units of m.

3.3. Spectral Analysis

The time series from each experiment is stationary after an initial period of transience. We remove the transient period and then pre-process the time series by applying mean subtraction and long-term linear detrending. The mean subtraction transforms the time series from absolute Q_s to Q_s deviation from the mean so that spectral power can be compared between experiments with different mean Q_s. The linear detrending removes any long-term shifts in Q_s to reduce long-term power growth in the spectra. Though we expect no trend in Q_s over long timescales, we apply this method as standard procedure.

Table 3
Model Parameter Values Used in Catchment Area Experiment Suites

			Value for model run				
Parameter	Symbol	Units	XS[a]	S[a]	M[a]	L[b]	XL[b]
Catchment area	A	km^2	4	9	16	25	100

[a]For extra small, small, and medium catchment area experiments, we only use the Base scenario values for t_{LS}, K_s, and V. [b]For large and extra large catchment area experiments, we ran the full suite of t_{LS}, K_s, and V values shown in Table 2.

We use the multi-taper method in the open-source *RedConf* package in MATLAB to generate spectral estimates of the time series of Q_s exiting the catchment for each experiment. The multi-taper method uses a series of orthogonal discrete prolate spheroidal sequences to taper the time series and averages the periodograms generated from each taper (Thomson, 1982; Weedon, 2003). We apply 5 tapers. This produces a smoothed spectral estimation, making it easier to pick out the changes in slope that mark the transition timescales, T_{RW} and T_{WB}. These timescales are identified using the *findchangepts* algorithm in MATLAB and rounded to the nearest 2 significant figures.

Table 4
Landscape Metrics for Model Runs in Which the Landslide Return Time (t_{LS}), Sediment Erodibility (K_s), or Net Effective Settling Velocity (V) Parameter are Varied

	Parameter values		Total relief		Threshold area		Hillslope gradient		Channel steepness	
			(m)	(MAD)	(m^2)	(MAD)	(Deg.)	(MAD)	(k_{sn})	(MAD)
Parameter being varied		Base scenario	803.7	±5.7	18,400	±1,200	43.1	±1.3	95	±8
Landslide return time	M	$t_{LS} = 1 \times 10^5$ y	825.5	±14.6	33,700	±12,100	54.6	±4.5	92	±20
	L	$t_{LS} = 1 \times 10^7$ y	818.4	±18.8	20,000	±3,600	76.1	±4.3	85	±5
Sediment erodibility	S	K_S 5×10^{-5} m^{-1}	1,084.2	±7.7	87,800	±5,400	43.7	±1.3	157	±33
	L	K_S 5×10^{-4} m^{-1}	436.6	±2.3	5,700	±100	43.1	±1.1	53	±1
Settling velocity	S	$V = 0.1$ m/y	580.8	±1.4	10,000	±300	43.1	±1.0	71	±5
	L	$V = 10$ m/y	1,742.8	±16.7	269,700	±43,000	42.0	±1.3	281	±74

Note. Reported values are the median and median absolute deviation.

4. Results

4.1. Landscape Morphological Changes

The base scenario landscape has a total catchment relief of 804 m. The threshold drainage area demarcating the transition from hillslope to fluvial processes is ~18,000 m^2. Median hillslope gradient is 43° and channel steepness, measured as k_{sn}, is 95 m. These metrics and their respective measures of variance are shown in Table 4.

Strong, but opposing trends appear when adjusting both K_s and V (Figure 2 & Table 4). Increasing V from 0.1 to 10 m/yr causes increases to relief, hillslope-channel threshold, and channel steepness. On the other hand, increasing K_s from 5×10^{-5} m^{-1} to 5×10^{-4} m^{-1} causes a decrease in relief, a decrease to hillslope-channel threshold, and a decrease to k_{sn}. Hillslope gradient, however, remains at ~43° regardless of the value used for either K_s or V.

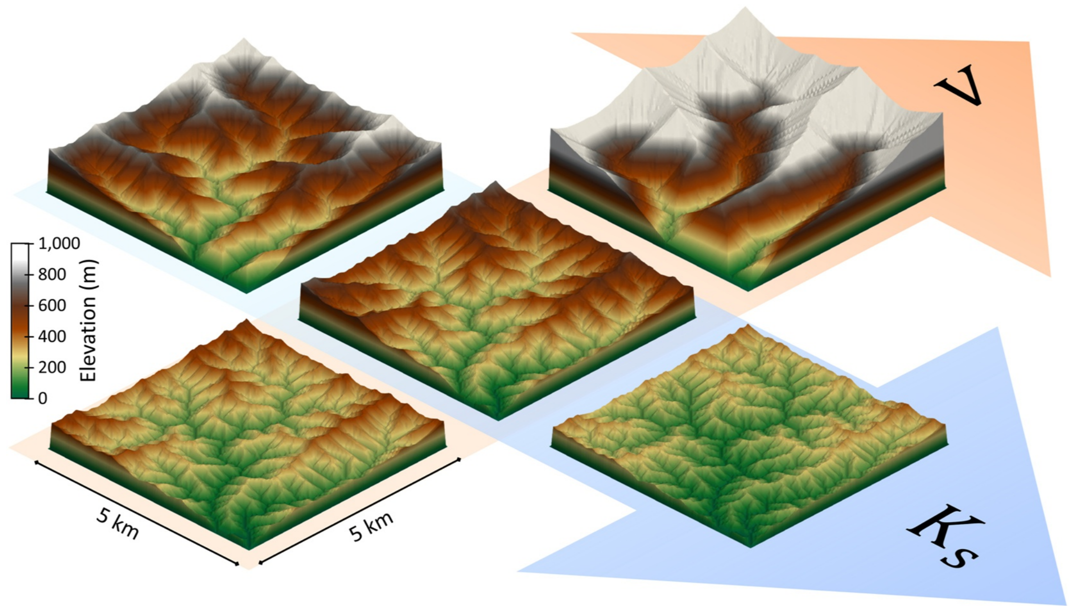

Figure 2. Topographic surface visualizations for the five scenarios in which the K_s or V parameter is varied. The middle landscape is the base scenario (parameter values of $t_{LS} = 1 \times 10^3$ years, $K_s = 5 \times 10^{-5}$ m^{-1}, and $V = 1$ m/yr). The arrows indicate the direction of increase for values of K_s (by 0.5 orders of magnitude between adjacent landscapes) and V (by one order of magnitude between adjacent landscapes).

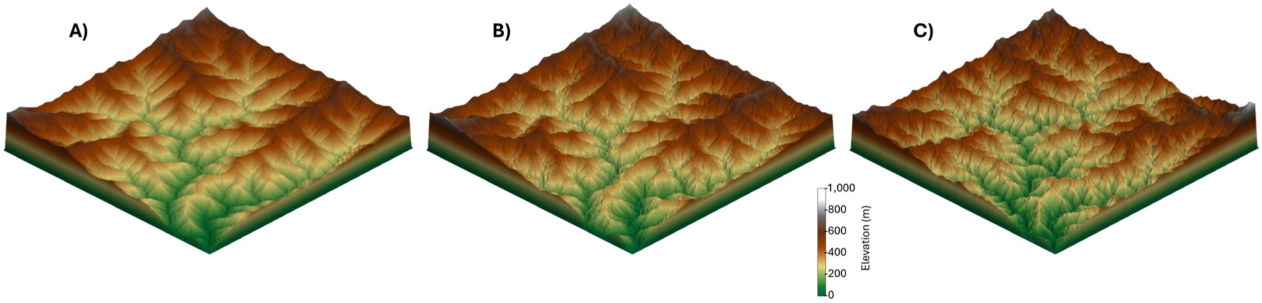

Figure 3. Topographic surface visualizations for the three scenarios in which the t_{LS} parameter is varied. Landslide frequency decreases as t_{LS} increases from left to right: (a) $t_{LS} = 1 \times 10^3$ years (base scenario), (b) $t_{LS} = 1 \times 10^5$ years, (c) $t_{LS} = 1 \times 10^7$ years.

Varying landslide return time, t_{LS}, across 4 orders of magnitude (from 10^3 to 10^7 years), while keeping the same base scenario K_s and V, has a different effect for each landscape metric. Total catchment relief varies only slightly (ranging from 804 to 826 m) and not systematically with t_{LS}. Mean hillslope gradient undergoes a strong increase as t_{LS} is increased. Increasing t_{LS} causes a slight decrease in k_{sn}. Finally, the threshold drainage area metric is greatly reduced from ~34,000 to ~20,000 m^2 when either increasing or decreasing t_{LS}. Figure 3 shows the final timestep of the three model scenarios in which t_{LS} is varied.

Increasing catchment size causes an increase in total relief but does not affect hillslope gradient or channel steepness (Table 5, Figure 4). Threshold drainage area also remains relatively unchanged for the four smallest (XS, S, M, L) catchments but is notably higher for the largest (XL) catchment (Table 5). This outlying value is likely an artifact of the calculation method—when compared to the smaller catchments, the XL catchment has many more datapoints in the large-area portion of the slope-area relationship, which changes the fit of the regressions and pushes the breakpoint to a larger value.

4.2. Time Series and Power Spectral Estimates

On average, over the course of an entire dynamic steady-state model run, the volumetric rate of sediment export from the catchment is equal to the rate of volume input from rock uplift ($Q_s = U \times A$, where A is catchment area). As such, large catchments export more sediment than small ones. Each time series of Q_s export comprises stochastic variations around this mean deterministic value. As described earlier, we normalize each time series by subtracting the long-term rate of volume input, resulting in time series of flux anomaly from the mean. We present two time series for each model scenario: one encompassing the first 2 million years of Q_s export from the catchment after the landscape has reached dynamic steady state (Figures 5–8d–8f) and another showing a representative snapshot of 20,000 years to zoom in to specific visual differences between model scenarios (Figures 5–8g–8i).

We also show the power spectra generated from the full 20-million-year dynamic steady state Q_s anomaly time series (Figures 5–8j–8l). From these power spectra, we focus primarily on the transition timescales T_{RW} and T_{WB}.

Table 5
Landscape Metrics for Model Runs in Which Catchment Area is Varied

Parameter being varied	Parameter values		Total relief (m)	(MAD)	Threshold area (m^2)	(MAD)	Hillslope gradient (Deg.)	(MAD)	Channel steepness (k_{sn})	(MAD)
Catchment area	XS	$A = 4$ km^2	566.8	±14.2	29,350	±7,100	52.7	±5.4	94	±14
	S	$A = 9$ km^2	692.8	±21.2	29,400	±4,900	52.6	±5.4	94	±16
	M	$A = 16$ km^2	778.3	±17.5	32,800	±7,300	52.6	±5.5	95	±16
	L (base scenario)	$A = 25$ km^2	825.5	±25.5	33,600	±12,200	52.6	±5.4	93	±15
	XL	$A = 100$ km^2	924.8	±46.2	43,300	±5,300	52.6	±5.4	94	±14

Note. Reported values are the median and median absolute deviation.

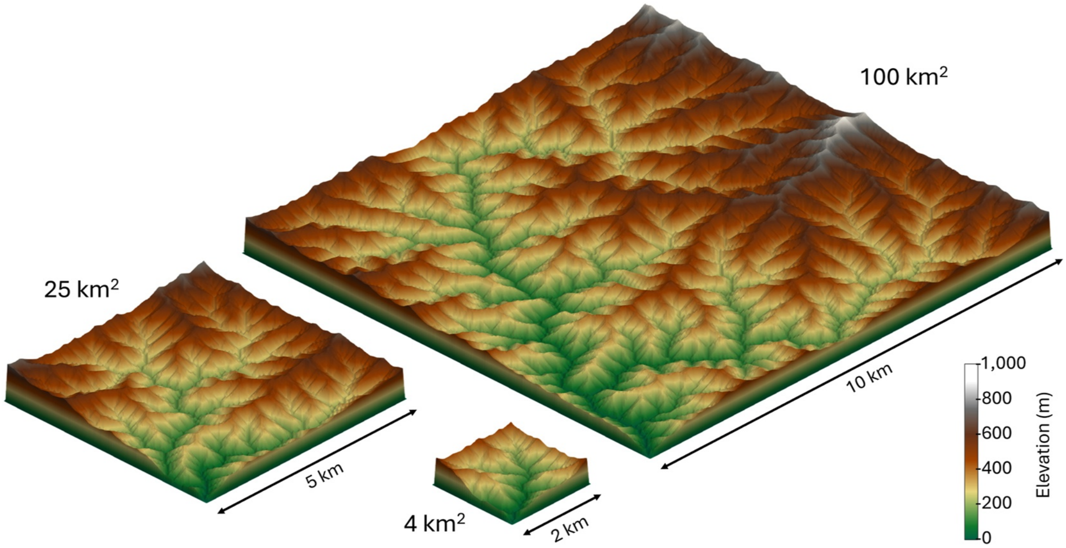

Figure 4. Comparison of three landscapes differing only in the size of the numerical domain. All three landscapes use base scenario parameters ($t_{LS} = 1 \times 10^3$ years, $K_s = 5 \times 10^{-5}$ m^{-1}, and $V = 1$ m/yr).

Figures 5–8 illustrate the spectral power across time scales less than 200,000 years. Over longer time scales, many scenarios exhibit a substantial increase in power. These may be caused by long-term rearrangement of the landscape through drainage divide migrations and/or sudden changes to the local base level of sub-catchments. Scenarios with more obvious and frequent large-scale rearrangements exhibit greater power increases at long timescales. The focus of this paper is on the shorter-term internal dynamics of sediment transport processes, so we do not elaborate any further. Figures showing the full range of timescales are available in the Supporting Information S1 (Figures S3–S6), as well as 3-dimensional time-lapse visualizations that show the dynamic rearrangement of sub-basins in some model runs.

Changing t_{LS} causes notable visual changes to the Q_s anomaly time series (Figures 5d–5i). When t_{LS} is small, there is a tight spread in Q_s anomalies between approximately −5 and +5 m^3/y. In the moderate-t_{LS} scenario, spikes are introduced where Q_s rises much higher than the background rate. In the high-t_{LS} scenario, the time between stochastic variations increases and a quasi-periodic drift emerges, where Q_s rises and falls over the course of hundreds of thousands of years. The power spectra for all three scenarios exhibit a red noise regime over short timescales that rolls over to white noise at longer timescales (Figures 5j–5l). This transition (T_{RW}) is distinct for the low-t_{LS} scenario but loses its sharpness and is difficult to attribute to an exact timescale as t_{LS} increases. Regardless, it is clear that T_{RW} increases as t_{LS} increases (Table 6). The transition from white to blue noise (T_{WB}) also increases with increasing t_{LS} (Table 6). The low frequency landsliding scenario does not exhibit a blue noise regime within the 200,000-year timescale covered by its power spectrum.

Previously, in Section 4.1, we showed that K_s and V control landscape form in a similar but opposite manner to each other. The same is true for their effect on sediment outflux from the catchment (Table 6, Figures 6 and 7). Decreasing K_s from the base scenario steepens the landscapes and results in more frequent large positive anomalies (Figures 6d and 6g) caused by increased landslide activity. This same effect occurs when increasing V (Figures 7f and 7i). Increasing K_s from the base scenario causes minimal visual change to the 2-million-year Q_s anomaly time series (Figure 6f) but shows higher frequency variations in Q_s over shorter timescales (Figure 6i). The same occurs when decreasing V, though without a clear visual change over short timescales (Figures 7d and 7g). In power spectral space, these differences manifest as a shortening of T_{RW} as K_s increases (Table 6, Figures 6j–6l) or V decreases (Table 6, Figures 7j–7l). T_{WB} is not affected much in these scenarios except for an increase when K_s is high (Table 6), resulting in a power spectrum with a very wide white noise regime (Figure 6l).

Changing catchment size produces only minor differences in Q_s anomaly time series and power spectral estimates (Figure 8). T_{RW} occurs at ∼2,500–3,400 years and T_{WB} occurs at ∼15,000–30,000 years (Table 7).

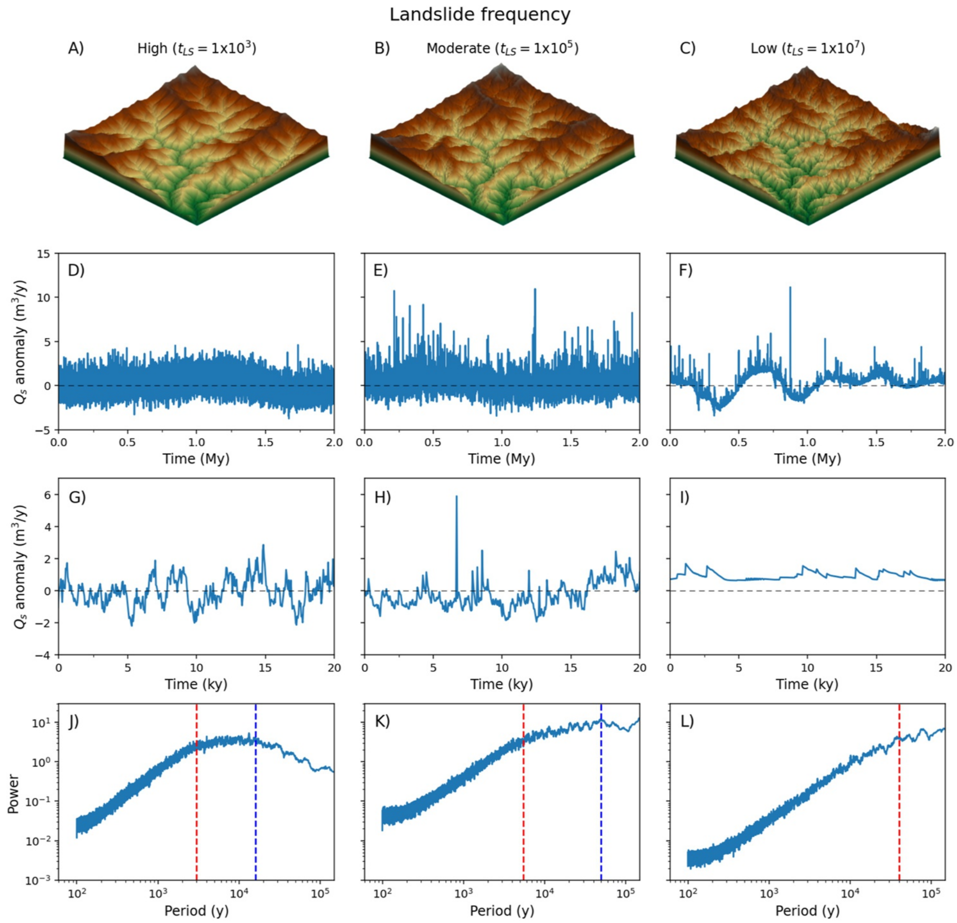

Figure 5. A comparison of landscapes, time series, and power spectra for the scenarios in which landslide return time, t_{LS}, is varied. From left to right, the columns show outputs for the high-t_{LS} scenario, the moderate-t_{LS} scenario, and the low-t_{LS} scenario, respectively. The top row (a, b, c) shows a 3-dimensional visualization of the landscape at the end of the 20-million-year model run. The middle two rows show time series of the output sediment flux anomaly over two different timescales: 2 million years (d, e, f), to visualize long-term characteristics of the time series, and 20 thousand years (g, h, i), to visualize shorter-term Q_s fluctuations. The bottom row shows the power spectra generated by the full 20 million year Q_s anomaly time series (j, k, l). The red dashed line marks the transition timescales between red and white noise, T_{RW}. The blue dashed line marks the transition timescale between white and blue, T_{WB}. These power spectra are cut off at 200 thousand years to focus on the timescales of T_{RW} and T_{WB}.

5. Interpretation of Model Process Dynamics

Before addressing the key questions about signal propagation and preservation, we first describe the internal process interactions created by the model to establish the numerical landscape as a complete dynamic system. We then characterize the noise in Q_S output from the catchment and gain information about the internal processes by analyzing the morphology, the Q_S anomaly time series, and the Q_S power spectra from each model scenario.

5.1. Landslide Frequency and Landscape Dynamism

When t_{LS} is high, landslides occur infrequently. Few landslide events, if any, occur concurrently and there is plenty of time between successive events for hillslopes to steepen greatly and produce very large individual landslides. These events produce large spikes in Q_S export followed by a return toward the mean export rate (Figure 5f). The long quiescent periods between landslide events allow fluvial incision to completely remove landslide deposits and erode into the underlying bedrock, which, having been protected by the deposit for some time, often has developed a knickpoint (e.g., Campforts et al., 2020; Korup et al., 2006; Ouimet et al., 2007). The upstream landscape responds to knickpoint erosion, the Q_S export drifts and causes medium-term variations about

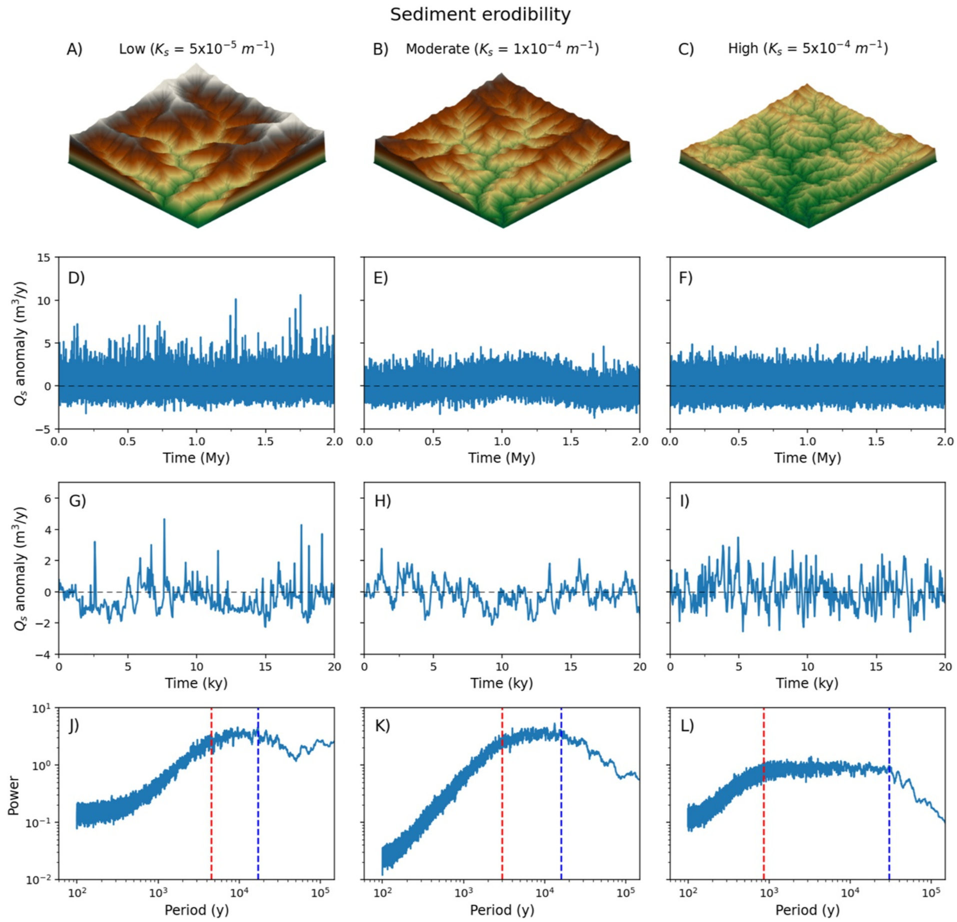

Figure 6. A comparison of landscapes, time series, and power spectra for the scenarios in which sediment erodibility, K_s, is varied. From left to right, the columns show outputs for the low-K_s scenario, the moderate-K_s scenario, and the high-K_s scenario, respectively. The top row (a, b, c) shows a 3-dimensional visualization of the landscape at the end of the 20-million-year model run. The middle two rows show time series of the output sediment flux anomaly over two different timescales: 2 million years (d, e, f), to visualize long-term characteristics of the time series, and 20 thousand years (g, h, i), to visualize shorter-term Q_s fluctuations. The bottom row shows the power spectra generated by the full 20 million year Q_s anomaly time series (j, k, l). The red dashed line marks the transition timescales between red and white noise, T_{RW}. The blue dashed line marks the transition timescale between white and blue, T_{WB}. These power spectra are cut off at 200 thousand years to focus on the timescales of T_{RW} and T_{WB}.

Table 6
Timescales Arising From Power Spectra for Model Runs in Which the Landslide Return Time (t_{LS}), Sediment Erodibility (K_s), or Net Effective Settling Velocity (V) Parameter are Varied

Parameter being varied		Parameter values Base scenario	T_{RW} (years) 3,000	T_{WB} (years) 16,000
Landslide return time	M	$t_{\mathrm{LS}} = 1 \times 10^5$ y	5,500	50,000
	L	$t_{\mathrm{LS}} = 1 \times 10^7$ y	40,000	*N*/A
Sediment erodibility	S	K_S 5 × 10^{-5} m^{-1}	4,500	17,000
	L	K_S 5 × 10^{-4} m^{-1}	850	30,000
Settling velocity	S	$V = 0.1$ m/y	2,200	20,000
	L	$V = 10$ m/y	4,700	19,000

the mean (undulations in Figure 5f). Because bedrock erosion is dominated by fluvial processes, the landscape comprises a valley network of relatively long, low-gradient river channels flanked by short, steep hillslopes primarily shaped by linear diffusion (Table 4 & Figure 3). Drainage density is high.

In contrast, when t_{LS} is low and landslides are frequent, bedrock erosion primarily occurs on the hillslopes. The landscape is dominated by lower-angle planar hillslopes caused by frequent landsliding (Figure 3). River channel steepness increases to more efficiently evacuate the abundant landslide material. The result is a total catchment relief that is similar to the high t_{LS} landscape, but channel steepness is higher, and hillslope gradient is lower (Table 4). This landscape produces a time series of Q_S anomaly with rapid low-magnitude fluctuations about the mean Q_S export rate (Figures 5d and 5g). The high frequency of landsliding causes many small landslides to occur simultaneously throughout the catchment. Between successive landslides,

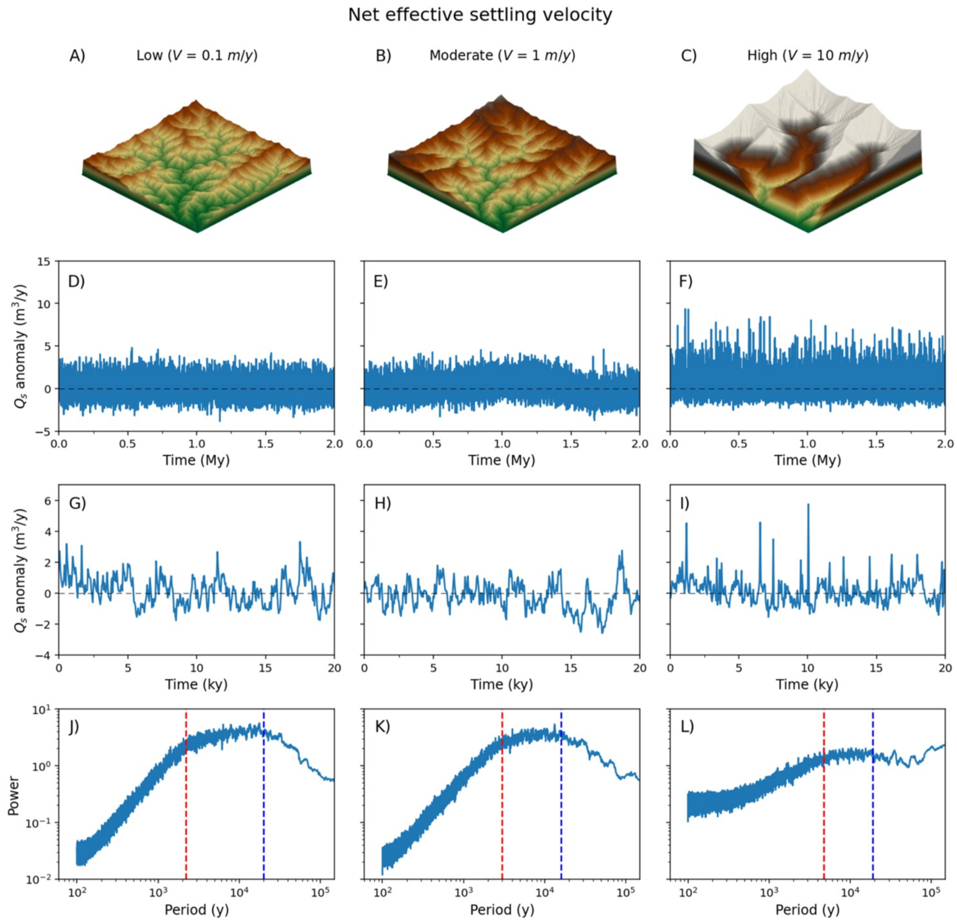

Figure 7. A comparison of landscapes, time series, and power spectra for the scenarios in which the net effective settling velocity parameter, V, is varied. From left to right, the columns show outputs for the low-V scenario, the moderate-V scenario, and the high-V scenario, respectively. The top row (a, b, c) shows a 3-dimensional visualization of the landscape at the end of the 20-million-year model run. The middle two rows show time series of the output sediment flux anomaly over two different timescales: 2 million years (d, e, f), to visualize long-term characteristics of the time series, and 20 thousand years (g, h, i), to visualize shorter-term Q_s fluctuations. The bottom row shows the power spectra generated by the full 20 million year Q_s anomaly time series (j, k, l). The red dashed line marks the transition timescales between red and white noise, T_{RW}. The blue dashed line marks the transition timescale between white and blue, T_{WB}. These power spectra are cut off at 200 thousand years to focus on the timescales of T_{RW} and T_{WB}.

hillslopes have little time to sufficiently steepen to generate extremely large events. The fluvial system constantly responds to new landslide deposits, so sediment export fluctuates rapidly.

These two scenarios offer clear end-member cases, between which lies the moderate-t_{LS} scenario that generates moderate hillslope gradient and channel steepness (Figure 3). Total relief is again similar, this time due to the combination of moderately steep channels with moderately angled hillslopes.

However, this does not tell the whole story. When t_{LS} is set to a moderate value, the two erosive processes are balanced (over the long term, they erode a roughly equal volume of bedrock), and the landscape becomes more dynamic as local erosive dominance shifts temporarily between the two processes. This dynamism creates high variability in channel steepness (high MAD, Table 4) due to local differences between bedrock reaches where slope is set by fluvial incision and temporarily over- or under-steepened reaches covered by landslide deposits. Variability in the threshold drainage area we use to partition hillslope and channel processes is also greatly increased in the moderate-t_{LS} scenario, indicating alternating dominance between hillslope and fluvial erosion of bedrock. The vigorous internal dynamics of the moderate-t_{LS} system cause larger magnitude changes in Q_S than those produced by individual landslides (Figure 5). There is likely enough time between landslides for hillslopes

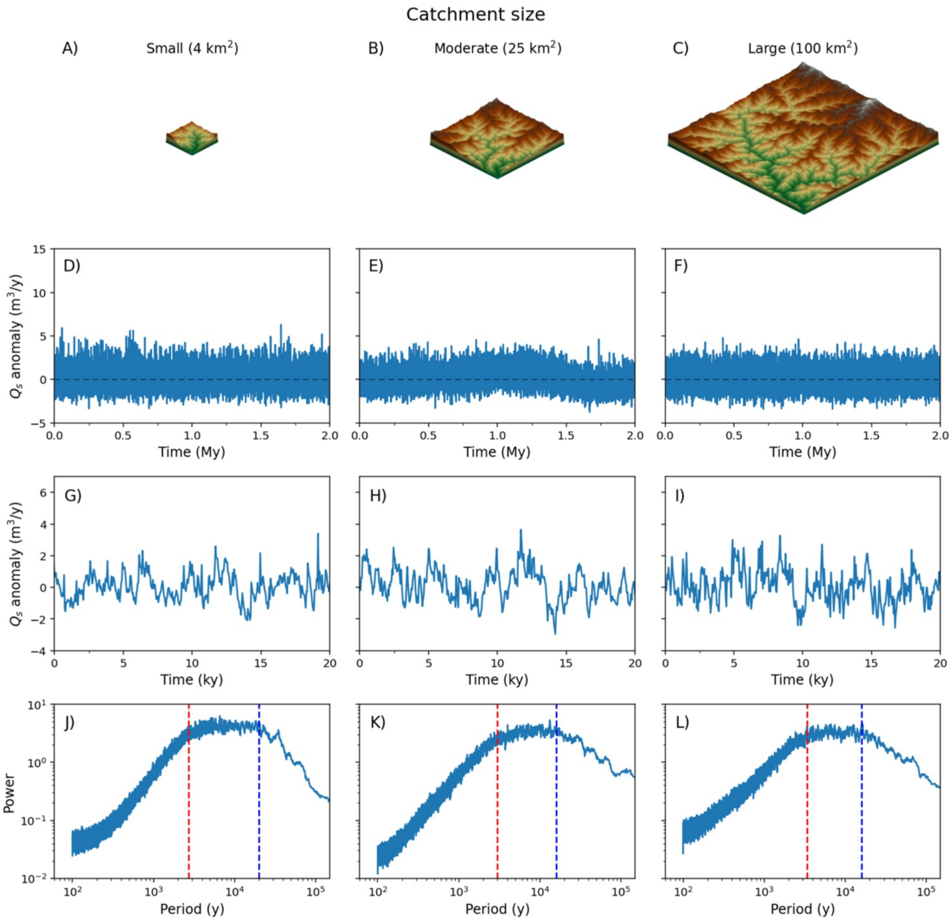

Figure 8. A comparison of landscapes, time series, and power spectra for the scenarios in which catchment area, A, is varied. From left to right, the columns show outputs for the XS scenario (4 km^2), the L scenario (25 km^2), and the XL scenario (100 km^2), respectively. The top row (a, b, c) shows a 3-dimensional visualization of the landscape at the end of the 20-million-year model run. The middle two rows show time series of the output sediment flux anomaly over two different timescales: 2 million years (d, e, f), to visualize long-term characteristics of the time series, and 20 thousand years (g, h, i), to visualize shorter-term Q_s fluctuations. The bottom row shows the power spectra generated by the full 20 million year Q_s anomaly time series (j, k, l). The red dashed line marks the transition timescales between red and white noise, T_{RW}. The blue dashed line marks the transition timescale between white and blue, T_{WB}. These power spectra are cut off at 200 thousand years to focus on the timescales of T_{RW} and T_{WB}.

to steepen such that large events rarely occur (and never occur with a shorter t_{LS}), but events are frequent enough throughout the landscape that several occur at the same time to generate extreme pulses of sediment discharge to the outlet.

Table 7
Timescales Arising From Power Spectra for Model Runs in Which Catchment Area is Varied

Parameter being varied	Parameter values		T_{RW} (years)	T_{WB} (years)
Catchment area	VS	$A = 4$ km^2	2,700	20,000
	S	$A = 9$ km^2	3,000	30,000
	M	$A = 16$ km^2	2,500	15,000
	L (base scenario)	$A = 25$ km^2	3,000	16,000
	VL	$A = 100$ km^2	3,400	16,000

Note. The transition between noise regimes is not always abrupt, so the approximate middle of the transition is reported.

5.1.1. Threshold Drainage Area

At every model timestep, the model calculates the volume of bedrock eroded by fluvial processes, and this volume increases with increasing t_{LS}. This indicates that more of the landscape is fluvially dominated as landslide return time increases, which is counter to the threshold drainage area values shown in Table 4. These values suggest that drainage density is highest when the landslide recurrence interval is shortest. We find that breakpoint analysis from slope-area data does not always result in critical drainage areas that correctly correlate with drainage density trends based on bedrock removed from fluvial incision. We hypothesize this is due to the dynamism of these landscapes. Landslides continually deposit sediment into the channels, leading to scattering in the slope-area data. This scatter, depending on where in the drainage network the deposit occurs, can impact calculated channel concavity and threshold drainage area, and is especially prominent in the moderate-t_{LS} scenario, in which the balance between fluvial and landslide processes is at its most dynamic.

5.2. Sediment Mobility and Hillslope-Channel Connectivity

The effects of the push-and-pull between the two process domains are further exaggerated when varying K_s and V. Both are parameters that affect sediment mobility and therefore the ability of the rivers to entrain or transport landslide-derived material.

Increasing V causes fluvially entrained material to quickly drop out of suspension and deposit back onto the channel bed. This effectively shortens the travel distance of entrained material and can represent, for example, increasing the mean grain size of entrained landslide-derived material. The river spends less of its erosive capacity incising into bedrock to instead re-entrain material that drops out of suspension. Channel steepness increases to compensate for the river's relative inability to evacuate sediment from the catchment (Figure 2). The steep landscape is highly prone to landslides, as there are many grid nodes that meet or exceed the "critical node" criteria. Regardless of the temporal probability set by the t_{LS} parameter, the high spatial probability of landslide occurrence drives frequent landsliding on these hillslopes. The drainage density is low, as reflected by long planar hillslopes that efficiently move bedrock downslope to the valley bottom. This material further armors the bedrock against fluvial incision. These two effects combine to increase total catchment relief (Table 4 & Figure 2). A similar effect is seen when decreasing the erodibility, K_s, of the mobile regolith layer. Channels steepen in order to generate enough power to erode the regolith and hillslopes lengthen, resulting in high relief (Figure 2). This is seen in natural landscapes, where coarse sediment cover may inhibit fluvial bedrock incision and hillslope-derived coarse sediment can control channel steepness (e.g., Anderson et al., 2023; Johnson et al., 2009; Korup, 2006; Lai et al., 2021; Shobe et al., 2016; Thaler & Covington, 2016).

The steep, landslide-prone landscapes of the high-V and low-K_s scenarios generate high variability in Q_s (Figures 6d and 6g, Figures 7f and 7i). This is especially true when many landslides occur simultaneously and produce a large positive anomaly in sediment flux as many tributaries suddenly increase their sediment load.

On the other hand, as V is decreased (or K_s is increased), fluvial entrainment or sediment transport become more efficient. Channel steepness can remain low and the limited hillslope material from landsliding of short hillslopes can be easily entrained and evacuated from the catchment (Figure 2). The lower relief landscape generates fewer "critical nodes" on its short hillslopes, resulting in fewer concurrent landslides and a smaller variability in Q_s export from the catchment (Figures 6e, 6f, 6h, 6i, 7d, and 7g) and more frequent swings in Q_s over short timescales (Figure 6i). If K_s is sufficiently increased or V sufficiently decreased, the landscape can become entirely fluvially controlled because the landscape reaches a low-relief equilibrium state in which hillslopes are never sufficiently tall or steep to trigger a landslide. Despite holding t_{LS} constant, changing sediment mobility parameters can change landslide frequency, and even result in a completely quiescent and deterministic landscape in which the *BedrockLandslider* could be removed from the model without affecting the landscape.

5.3. Emergent Timescale of Correlation

Despite the visual differences in Q_s export when plotted in time, each time series share some common attributes in their power spectra (Figures 5–8j, 8k and 8l). All power spectra exhibit a red noise regime over short timescales that rolls over to white noise at longer timescales. This transition timescale (T_{RW}) occurs at approximately 3,000 years for the base scenario (Figures 5j, 6–8k, marked by the red dashed line). The red noise is caused by correlation in sediment export from the catchment. After a landslide, Q_s temporarily increases as the river entrains and evacuates the landslide deposit. This correlation lasts until the transition timescale, T_{RW}, from red noise to white noise. As such, T_{RW} scales with the residence time of landslide deposits.

This phenomenon is particularly clear when comparing different model scenarios. Increasing V decreases the distance that sediment is transported before being deposited, thus increasing both the transport time for sediment to exit the catchment and slowing the rate of recruitment of new deposit material, as the river fills a larger fraction of its transport capacity by re-entraining alluvial material. These effects increase the residence time of deposits on the landscape and therefore increase the emergent timescale T_{RW} (from 2,200 to 2,500 to 4,700 years as V

increases, Table 6). Similarly, T_{RW} increases from 850 to 2,500 to 4,500 years as K_s decreases because landslide deposits become more difficult to erode and remain on the landscape for a longer time (Table 6). Reducing landslide frequency by increasing t_{LS} causes hillslopes to generate fewer, but larger landslides that deposit larger individual masses of sediment that take longer to erode, thus increasing the timescale for T_{RW}. The very long T_{RW} for the high-t_{LS} scenario is likely reflective of long-term correlation in Q_S as sub-basins respond to bedrock knickpoints uncovered from beneath the large deposits. In this case, the correlation extends beyond the timescale of landslide deposit erosion and also reflects the longer-term knock-on effect of knickpoint propagation.

5.4. Recharge Timescale

In addition to the emergent T_{RW}, most of the power spectra exhibit a transition from white to blue noise (T_{WB}, Figures 5j, 6–8j–8l) and therefore follow the tripartite power spectrum framework described in Griffin et al. (2023). For rice piles, T_{WB} represents a regeneration timescale, which is the time required for mass influx to replenish the mass lost in the largest failure events. This is determined by the size of these "system clearing events" and by the rate of mass influx. Following this logic, T_{WB} in the numerical model scenarios should reflect the time it takes to "recharge" a hillslope after a large "slope-clearing" landslide. The hillslope must steepen before failing again, so T_{WB} should scale as a function of both event size and hillslope recharge rate. This recharge rate should be roughly the same in each scenario, as it is dependent on the rock uplift rate (held constant) and on the hillslope-steepening process of fluvial incision at the toe of the slope (at long-term equilibrium with the rock uplift rate). T_{WB} should therefore reflect the elevation change caused by the largest potential landslide in each scenario. The less frequently a hillslope is subject to landsliding, the more time it has to steepen. This is indeed the case; the low-t_{LS} scenario has frequent landslides and a short T_{WB} (13,000 years), the moderate-t_{LS} scenario has less frequent landslides and a longer T_{WB} (50,000 years), and the high-t_{LS} scenario has infrequent landslides and there is no indication of T_{WB} occurring over the 200,000-year periodicity covered by the power spectrum. The scenarios in which we vary K_s and V but hold t_{LS} constant show no clear trend in T_{WB}.

5.5. Catchment Size and Self-Similarity

Before performing our experiments, we had hypothesized that larger watersheds, which have a longer internal transport system, would be more likely to degrade signals. Increasing the size of the catchment increases the mean sediment flux rate, but it does not greatly change the character of the flux anomalies about the mean (Figures 8d–8i) or the power spectra, T_{RW}, or T_{WB} (Figures 8j–8l, Table 7). This is because the numerical domain is entirely erosional (on average) and generates a self-similar river network and topographic surface for any size larger than one valley width (Figure 4). The self-similarity is revealed through landscape metrics; though total catchment relief increases with increasing catchment area (relief is a function of the length of the longest river channel), neither channel steepness nor hillslope gradient is affected (Table 5). All regions of the watershed behave in the same manner; there is no transfer zone in which noise from landslides could be muted or buffered as sediment is stored and remobilized (Figure 4). In natural landscapes, large watersheds can encompass portions of the core of a mountain range, where landslides might be more likely to occur, as well as lower-relief foothills and alluvial plains, where upstream sediment is deposited and remobilized over time. As the character of the landscape changes, its ability to transmit or degrade signals will also change, even if there are no drastic changes in the geomorphic processes at play. Future simulations exploring spatially variable boundary conditions (e.g., U) or parameters (e.g., K_s) may provide new insights.

6. Discussion

In this study, we use landslides as an autogenic stochastic process to generate noise in sediment efflux from catchments shaped by spatially invariant parameters under uniform uplift. The modeled landscapes are not meant to exactly represent a real-world study site, but to produce results from which we can draw general conclusions about signal propagation and degradation in natural systems.

Our key finding is that an emergent correlation timescale arises from the coupling of distinct sediment transport processes and their combined effects on landscape evolution. Prior work has shown that environmental signals with a period up to the correlation timescale (T_{RW}) of stochastic sediment flux (Q_s) are especially prone to shredding (Griffin et al., 2023; Jerolmack & Paola, 2010), yet the origin of such long correlation timescales in erosional landscapes has remained unclear. In isolation, neither of the processes modeled here can generate correlation in Q_s through time. Landslides are effectively instantaneous events, both in nature and as represented in our model, and therefore do not impart temporal memory. Fluvial entrainment and transport as modeled under steady forcing, evolve toward a static steady state in which Q_s is constant through time (Shobe et al., 2017). Correlation occurs only when these processes are dynamically linked. Specifically, landslides deliver discrete pulses of sediment from hillslopes to valley bottoms, creating transient, erodible deposits that are subsequently reworked by the fluvial system over timescales of centuries to millennia. It is the coupling between stochastic sediment delivery and deterministic fluvial reworking that generates a previously unrecognized geologically relevant correlation timescale. This result provides a mechanistic foundation for predicting which environmental signals are likely to be preserved, attenuated, or shredded as they propagate through sediment routing systems.

Our results demonstrate that the structure of Q_s variability, and its diagnostic expression in power spectra, is fundamentally governed by process coupling, providing a unifying framework that extends well beyond previously studied single-process systems (e.g., Ganti et al., 2024; Griffin et al., 2023; Jerolmack & Paola, 2010). In this context, the tripartite framework for characterizing Q_s power spectra developed by Griffin et al. (2023) can be extended from quasi-one-dimensional rice pile experiments to fully two-dimensional systems, and from single-process dynamics to landscapes in which multiple sediment transport processes interact. More broadly, there is no clear reason this framework should not be applicable to three-dimensional systems, systems with additional interacting processes, or real-world sediment routing systems. For example, introducing lateral river meandering (e.g., Kwang et al., 2021; Langston & Tucker, 2018) into the LEM would add a new stochastic process in the form of meander cutoffs. Although individual cutoff events occur over short timescales, they can induce longer-lived adjustments by triggering further erosion that mobilizes floodplain sediments and increases Q_s export over extended periods (e.g., Fuller et al., 2009; Hooke, 1995; Macar, 1934; Zinger et al., 2011). This behavior could give rise to an additional emergent correlation timescale independent of landsliding. Furthermore, new feedbacks can arise between meandering and landsliding processes: meander bends can erode hillslope toes and trigger landslides, while landslide deposits can deflect channels, promoting further erosion, cutoff formation, and hillslope destabilization (Ahrendt et al., 2025; Larsen & Montgomery, 2012). Despite this added complexity, we expect that key emergent timescales would continue to manifest in Q_s power spectra. Characterizing these key timescales allows us to understand the signal transmission capability of a given sediment transport system.

For a Q_s signal to become preserved in strata, it needs to reach the depositional environment intact and then survive depositional processes before it is sufficiently buried and insulated from erosion (Sifuentes et al., 2025). Our results show that even if the depositional environment is favorable to the preservation of high-frequency signals, the transit path between the source and sink may act as a low-pass filter that degrades signals in transmission. Furthermore, it is plausible that interactions between sediment transport processes may elongate the low-pass filter to timescales longer than the longest individual process timescale in the sediment routing system.

We now discuss these general findings in relation to our specific LEM and to examples of natural systems. In our simulations, we interpret T_{RW} to be related to the residence time of landslide deposits, suggesting that hillslope and channel sediment cover may be a first-order metric for estimating whether a given catchment is more likely to transmit a signal than another. We find that T_{RW}—the time it takes to evacuate landslide deposits from the catchment—decreases (Table 6) as sediment becomes more erodible (larger K_s, Figure 6) or more easily transported (smaller V, Figure 7). Thus, field settings in regions composed of highly erodible, fine-grained materials might allow transmission of relatively short timescale signals. An example of such a setting is the Loess Plateau, China. The Yellow River, which drains the Loess Plateau, has the highest suspended sediment load of all major world rivers (Milliman & Meade, 1983). A sudden input of hillslope-derived loess (large K_s, small V) to the fluvial system would likely be entrained and transported a long distance downstream over a short period of time, quickly leaving the erosional catchment. This individual event may create a short-term spike in Q_s before the affected reach returns to a local equilibrium. Moderate timescale Q_s changes caused by cyclical environmental forcing may last longer than the noisy spike and therefore survive the degradation potential of such sudden events. On the other hand, regions where hillslopes supply channels with larger caliber sediment (large V) or erosion-resistant rock (small K_s) may act as a low-pass filter and allow only long-period signals to pass down-system. For example, in Taiwan, a sudden input of hillslope-derived sediment to the channel may take centuries to erode (DeLisle et al., 2022). During this period, the same oscillations in Q_s that may have been detected in a loess-dominated environment would oscillate through several full cycles while Q_s export from the catchment remains elevated from the landslide-derived sediment pulse. The cyclical signal may become degraded during this time and perhaps render it undetectable to power spectral analysis. This aligns with research from depositional environments showing that fine-grained deposits can preserve shorter cyclical signals than coarse-grained deposits (Yang et al., 2024).

We refrain from relating the exact correlation timescales measured in our simulations to those of natural phenomena, as the model does not account for sediment entrainment thresholds and variable fluvial discharge (Adams et al., 2017; Coulthard et al., 2013; Deal et al., 2018; DiBiase & Whipple, 2011; Lague et al., 2005; e.g., Paola et al., 1992; Snyder et al., 2003; Tucker, 2004; Zhang et al., 2015), and some parameters cannot be directly calibrated from field measurements (e.g., the V term behaves like a settling velocity, but its value is orders of magnitude smaller than any settling velocity that would be measured in nature). However, it is worth noting that the correlation timescales range from approximately 10^3 years to well in excess of 10^4 years. This range encompasses or exceeds some commonly discussed cyclical environmental forcings of interest to the scientific community. For example, though all of the simulations would likely transmit major climate cycles of the order of 100,000+ years (e.g., orbital eccentricity), and some could potentially transmit the shorter Milankovitch cycles (e.g., axial tilt and precession), few would transmit millennial cycles (e.g., Dansgaard-Oeschger events and Bond cycles), and likely none would transmit decadal cycles such as the Pacific Decadal Oscillation or El Niño–Southern Oscillation.

In our simulated landscapes, we only explore the signature of volumetric sediment flux (Q_s) exported from the catchment without regard to grain size partitioning or chemical composition. In a natural system, smaller grain size fractions may be preferentially eroded from landslide deposits, and it is likely that the correlation timescale for finer grain sizes is shorter than that for larger grain sizes. For a given signal of interest, clearly characterizing the transport system can help to define the specific indicator that is minimally affected by the autogenic storage and release processes within that system. For example, a quiescent glacio-lacustrine environment can allow for deposition of seasonal varves that record interannual, decadal and centennial solar and climate cycles with minimal shredding due to the absence of confounding transport processes for fine-grained material within the system (Griffin et al., 2026). Searching for such signals in an environment subject to strong tides, currents, or waves would likely prove less successful. Characterization of transport systems should include analysis of process coupling, as our results show that sometimes process coupling can lead to far greater correlation timescales than would be expected from individual processes. The general framework presented here should likely hold for any physical tracer over timescales relevant to their transport pathway.

Our work here naturally motivates the next step: testing how external environmental signals are transmitted through erosional landscapes that possess emergent memory. Specifically, imposing cyclic forcing, such as oscillations in uplift rate or precipitation, across a range of timescales relative to the emergent correlation timescale (T_{RW}) provides a direct means of evaluating signal preservation versus shredding. Signals imposed at timescales longer than T_{RW} should be coherently transmitted through the system, whereas those imposed at shorter timescales should be attenuated or shredded by internally generated variability. Importantly, our results suggest that this threshold is not an inherent property of any single process but rather arises from process coupling, implying that it may shift systematically with changes in landscape dynamics, sediment supply, or transport efficiency that may occur during a forcing event. By explicitly linking forcing frequency to system memory, this approach offers a predictive framework for identifying which environmental signals can be reliably extracted from sedimentary archives, and which are likely to be obscured during transport

7. Conclusions

Allogenic sediment flux signals traveling from source to sink may become degraded by autogenic sediment transport processes below the key timescale of correlation. We explored the transmission potential of sediment flux signals in a coupled 2D LEM of stochastic landsliding and deterministic fluvial processes. We varied the landslide frequency, sediment erodibility, and fluvial transport length scale to generate various dynamic steady state scenarios. We analyzed model output to identify process signatures in landscape morphology (points 1 and 2, below) and the likelihood of signal preservation in the sediment flux (points 3 and 4, below). We find that:

1. The interplay of the two erosive processes generates a highly dynamic landscape. When fluvial incision is the primary process eroding bedrock, the landscape consists of long, low-gradient valleys flanked by short, steep hillslopes. When deep-seated landslides dominate bedrock erosion, the hillslopes are long, planar, and lie at a lower angle, while shorter, steeper channels more efficiently evacuate landslide-derived sediment. The more balanced the two processes are, the more dynamic the landscape—local erosive dominance shifts temporarily

between the two processes and results in highly variable channel steepness caused by frequent knickpoint generation where bedrock is protected by spatially dispersed landslide deposits.
2. Sediment-related parameters greatly affect the interplay between fluvial and hillslope processes. When fluvial processes erode and transport sediment more efficiently, the erosive dominance can shift toward fluvial incision. This reduces channel steepness and increases drainage density, which causes hillslopes to shorten and landslide frequency to decrease. On the other hand, when fluvial processes are less efficient, landslide-derived material builds up in the valleys (as it is not quickly evacuated) and armors the bedrock against fluvial incision. Channels steepen to compensate for their inefficiency, but the steeper landscape is more prone to landslides. A positive feedback loop occurs in which long planar hillslopes dominate the landscape, and the channels act as conveyers to evacuate landslide-derived sediment from the catchment.
3. An emergent timescale of correlation in the sediment efflux from the catchment arises from the internal dynamics caused by the coupling of hillslope and channel processes. Landslides provide instantaneous mass fluxes from hillslopes to channels that overwhelm the fluvial transport capacity, resulting in the protracted evacuation of the landslide deposits as the rivers erode them through time. Such correlation in sediment flux is known to degrade sedimentary signals as they travel (Griffin et al., 2023; Jerolmack & Paola, 2010). Landscapes with highly erodible sediment or highly efficient fluvial transport are more likely to transmit shorter-frequency signals because of shorter timescales of correlation.
4. Q_s power spectra from two-dimensional, multi-process sediment routing systems can be characterized using the same tripartite framework developed by Griffin et al. (2023) for quasi-one-dimensional, single-process rice pile experiments. The transitions between correlated (red) noise, uncorrelated (white) noise, and anti-correlated (blue) noise mark distinct timescales of change in the transport system's behaviors. Our results suggest that the framework should also be applicable to real-world sediment routing systems.

These results provide us with a better understanding of how the interactions between autogenic processes can impact signal degradation prior to export from erosional catchments. Identifying and quantifying the emergent correlation timescales arising from these interactions is important for predicting where paleo-tectonic and paleo-climatic signals may be preserved.

Conflict of Interest

The authors declare no conflicts of interest relevant to this study.

Availability Statement

The data (sediment flux timeseries and power spectra) and the python scripts used to run the LEM and make the figures for this study are available on Github (https://github.com/loroberge/pub_Roberge_et_al_LandslideFluvialSedSignal_JGR-ES) and Zenodo (Roberge, 2025). All simulations were run in Landlab version 2.9.2.

Acknowledgments
We are grateful for monetary support from U.S. National Science Foundation Grants EAR 2148506, OAC 2103815, and EAR 1904268.

References

Adams, J. M., Gasparini, N. M., Hobley, D. E. J., Tucker, G. E., Hutton, E. W. H., Nudurupati, S. S., & Istanbulluoglu, E. (2017). The landlab v1.0 OverlandFlow component: A python tool for computing shallow-water flow across watersheds. *Geoscientific Model Development*, *10*(4), 1645–1663. https://doi.org/10.5194/gmd-10-1645-2017

Ahrendt, S. M., Mirus, B. B., LaHusen, S. R., & Perkins, J. P. (2025). Dynamic feedbacks between river meandering and landsliding in Northwestern Washington glacial terraces. *Journal of Geophysical Research: Earth Surface*, *130*(8), e2024JF008249. https://doi.org/10.1029/2024JF008249

Allen, P. A. (2008). Time scales of tectonic landscapes and their sediment routing systems. *Geological Society*, *296*, 7–28. https://doi.org/10.1144/SP296.2

Anderson, S., Gasparini, N., & Johnson, J. (2023). Building a bimodal landscape: Bedrock lithology and bed thickness controls on the morphology of last chance canyon, New Mexico, USA. *Earth Surface Dynamics*, *11*(5), 995–1011. https://doi.org/10.5194/esurf-11-995-2023

Barnhart, K. R., Glade, R. C., Shobe, C. M., & Tucker, G. E. (2019). Terrainbento 1.0: A python package for multi-model analysis in long-term drainage basin evolution. *Geoscientific Model Development*, *12*(4), 1267–1297. https://doi.org/10.5194/gmd-12-1267-2019

Barnhart, K. R., Hutton, E. W. H., Tucker, G. E., Gasparini, N. M., Istanbulluoglu, E., Hobley, D. E. J., et al. (2020). Short communication: Landlab v2.0: A software package for Earth surface dynamics. *Earth Surface Dynamics*, *8*(2), 379–397. https://doi.org/10.5194/esurf-8-379-2020

Campforts, B., Shobe, C. M., Overeem, I., & Tucker, G. E. (2022). The art of landslides: How stochastic mass wasting shapes topography and influences landscape dynamics. *Journal of Geophysical Research: Earth Surface*, *127*(8), e2022JF006745. https://doi.org/10.1029/2022JF006745

Campforts, B., Shobe, C. M., Steer, P., Vanmaercke, M., Lague, D., & Braun, J. (2020). HyLands 1.0: A hybrid landscape evolution model to simulate the impact of landslides and landslide-derived sediment on landscape evolution. *Geoscientific Model Development*, *13*(9), 3863–3886. https://doi.org/10.5194/gmd-13-3863-2020

Castelltort, S., & Van Den Driessche, J. (2003). How plausible are high-frequency sediment supply-driven cycles in the stratigraphic record? *Sedimentary Geology*, *157*(1–2), 3–13. https://doi.org/10.1016/S0037-0738(03)00066-6

Clubb, F. J., Mudd, S. M., Milodowski, D. T., Hurst, M. D., & Slater, L. J. (2014). Objective extraction of channel heads from high-resolution topographic data. *Water Resources Research*, *50*(5), 4283–4304. https://doi.org/10.1002/2013WR015167

Coulthard, T. J., Neal, J. C., Bates, P. D., Ramirez, J., de Almeida, G. A. M., & Hancock, G. R. (2013). Integrating the LISFLOOD-FP 2D hydrodynamic model with the CAESAR model: Implications for modelling landscape evolution. *Earth Surface Processes and Landforms*, *38*(15), 1897–1906. https://doi.org/10.1002/esp.3478

Davy, P., & Lague, D. (2009). Fluvial erosion/transport equation of landscape evolution models revisited. *Journal of Geophysical Research*, *114*(F3), 2008JF001146. https://doi.org/10.1029/2008JF001146

Deal, E., Braun, J., & Botter, G. (2018). Understanding the role of rainfall and hydrology in determining fluvial erosion efficiency. *Journal of Geophysical Research: Earth Surface*, *123*(4), 744–778. https://doi.org/10.1002/2017JF004393

DeLisle, C., Yanites, B. J., Chen, C.-Y., Shyu, J. B. H., & Rittenour, T. M. (2022). Extreme event-driven sediment aggradation and erosional buffering along a tectonic gradient in southern Taiwan. *Geology*, *50*(1), 16–20. https://doi.org/10.1130/G49304.1

DiBiase, R. A., & Whipple, K. X. (2011). The influence of erosion thresholds and runoff variability on the relationships among topography, climate, and erosion rate. *Journal of Geophysical Research*, *116*(F4), F04036. https://doi.org/10.1029/2011JF002095

Frette, V., Christensen, K., Malthe-Sørenssen, A., Feder, J., Jøssang, T., & Meakin, P. (1996). Avalanche dynamics in a pile of rice. *Nature*, *379*(6560), 49–52. https://doi.org/10.1038/379049a0

Fuller, T. K., Perg, L. A., Willenbring, J. K., & Lepper, K. (2009). Field evidence for climate-driven changes in sediment supply leading to strath terrace formation. *Geology*, *37*(5), 467–470. https://doi.org/10.1130/G25487A.1

Ganti, V., Kelley, M. M., Das, D., & Mahon, R. C. (2024). Timescales of autogenic noise in river bedform evolution and stratigraphy. *Geophysical Research Letters*, *51*(11), e2024GL108965. https://doi.org/10.1029/2024GL108965

Godard, V., Tucker, G. E., Burch Fisher, G., Burbank, D. W., & Bookhagen, B. (2013). Frequency-dependent landscape response to climatic forcing. *Geophysical Research Letters*, *40*(5), 859–863. https://doi.org/10.1002/grl.50253

Griffin, C., Duller, R. A., & Straub, K. M. (2023). The degradation and detection of environmental signals in sediment transport systems. *Science Advances*, *9*(44), eadi8046. https://doi.org/10.1126/sciadv.adi8046

Griffin, C., Duller, R. A., & Straub, K. M. (2024). The incomplete record of autogenic processes sets limits on signal detectability. *Journal of Geophysical Research: Earth Surface*, *129*(4), e2023JF007538. https://doi.org/10.1029/2023JF007538

Griffin, C., Gernon, T. M., Fu, M., Rugen, E. J., Spencer, A. M., Warrington, G., & Hincks, T. K. (2026). Interannual to multidecadal climate oscillations occurred during Cryogenian glaciation. *Earth and Planetary Science Letters*, *679*, 119891. https://doi.org/10.1016/j.epsl.2026.119891

Hobley, D. E. J., Adams, J. M., Nudurupati, S. S., Hutton, E. W. H., Gasparini, N. M., Istanbulluoglu, E., & Tucker, G. E. (2017). Creative computing with landlab: An open-source toolkit for building, coupling, and exploring two-dimensional numerical models of Earth-surface dynamics. *Earth Surface Dynamics*, *5*(1), 21–46. https://doi.org/10.5194/esurf-5-21-2017

Hooke, J. M. (1995). River channel adjustment to meander cutoffs on the river bollin and river dane, northwest England. *Geomorphology*, *14*(3), 235–253. https://doi.org/10.1016/0169-555X(95)00110-Q

Hwa, T., & Kardar, M. (1992). Avalanches, hydrodynamics, and discharge events in models of sandpiles. *Physical Review A*, *45*(10), 7002–7023. https://doi.org/10.1103/PhysRevA.45.7002

Jerolmack, D. J., & Paola, C. (2010). Shredding of environmental signals by sediment transport. *Geophysical Research Letters*, *37*(19), 2010GL044638. https://doi.org/10.1029/2010GL044638

Johnson, J. P. L., Whipple, K. X., Sklar, L. S., & Hanks, T. C. (2009). Transport slopes, sediment cover, and bedrock channel incision in the henry Mountains, Utah. *Journal of Geophysical Research*, *114*(F2). https://doi.org/10.1029/2007JF000862

Korup, O. (2006). Rock-slope failure and the river long profile. *Geology*, *34*(1), 45–48. https://doi.org/10.1130/G21959.1

Korup, O., Strom, A. L., & Weidinger, J. T. (2006). Fluvial response to large rock-slope failures: Examples from the Himalayas, the tien Shan, and the Southern alps in New Zealand. *Geomorphology*, *78*(1–2), 3–21. https://doi.org/10.1016/j.geomorph.2006.01.020

Kwang, J. S., Langston, A. L., & Parker, G. (2021). The role of lateral erosion in the evolution of nondendritic drainage networks to dendricity and the persistence of dynamic networks. *Proceedings of the National Academy of Sciences*, *118*(16), e2015770118. https://doi.org/10.1073/pnas.2015770118

Lague, D., Hovius, N., & Davy, P. (2005). Discharge, discharge variability, and the bedrock channel profile. *Journal of Geophysical Research*, *110*(F4). https://doi.org/10.1029/2004JF000259

Lai, L. S.-H., Roering, J. J., Finnegan, N. J., Dorsey, R. J., & Yen, J.-Y. (2021). Coarse sediment supply sets the slope of bedrock channels in rapidly uplifting terrain: Field and topographic evidence from eastern Taiwan. *Earth Surface Processes and Landforms*, *46*(13), 2671–2689. https://doi.org/10.1002/esp.5200

Langston, A. L., & Tucker, G. E. (2018). Developing and exploring a theory for the lateral erosion of bedrock channels for use in landscape evolution models. *Earth Surface Dynamics*, *6*(1), 1–27. https://doi.org/10.5194/esurf-6-1-2018

Larsen, I. J., & Montgomery, D. R. (2012). Landslide erosion coupled to tectonics and river incision. *Nature Geoscience*, *5*(7), 468–473. https://doi.org/10.1038/ngeo1479

Li, Q., Gasparini, N. M., & Straub, K. M. (2018). Some signals are not the same as they appear: How do erosional landscapes transform tectonic history into sediment flux records? *Geology*, *46*(5), 407–410. https://doi.org/10.1130/G40026.1

Macar, P. F. (1934). Effects of cut-off meanders on the longitudinal profiles of Rivers. *The Journal of Geology*, *42*(5), 523–536. https://doi.org/10.1086/624197

Mason, C. C., Romans, B. W., Stockli, D. F., Mapes, R. W., & Fildani, A. (2019). Detrital zircons reveal sea-level and hydroclimate controls on amazon river to deep-sea fan sediment transfer. *Geology*, *47*(6), 563–567. https://doi.org/10.1130/G45852.1

McNeill, L. C., Shillington, D. J., Carter, G. D. O., Everest, J. D., Gawthorpe, R. L., Miller, C., et al. (2019). High-resolution record reveals climate-driven environmental and sedimentary changes in an active rift. *Scientific Reports*, *9*(1), 3116. https://doi.org/10.1038/s41598-019-40022-w

Milliman, J. D., & Meade, R. H. (1983). World-wide delivery of river sediment to the oceans. *The Journal of Geology*, *91*(1), 1–21. https://doi.org/10.1086/628741

Ouimet, W. B., Whipple, K. X., Royden, L. H., Sun, Z., & Chen, Z. (2007). The influence of large landslides on river incision in a transient landscape: Eastern margin of the Tibetan Plateau (sichuan, China). *Geological Society of America Bulletin*, *119*(11–12), 1462–1476. https://doi.org/10.1130/B26136.1

Paola, C., Heller, P. L., & Angevine, C. L. (1992). The large-scale dynamics of grain-size variation in alluvial basins, 1: Theory. *Basin Research*, *4*(2), 73–90. https://doi.org/10.1111/j.1365-2117.1992.tb00145.x

Pavano, F., Pazzaglia, F. J., & Catalano, S. (2016). Knickpoints as geomorphic markers of active tectonics: A case study from northeastern sicily (southern Italy). *Lithosphere*, *8*(6), 633–648. https://doi.org/10.1130/L577.1
Pavano, F., Pazzaglia, F. J., Rittenour, T. M., Catalano, S., Corbett, L. B., & Bierman, P. (2024). Integrated uplift, subsidence, erosion and deposition in a tightly coupled source-to-sink system, pagliara basin, northeastern Sicily, Italy. *Basin Research*, *36*(1), e12845. https://doi.org/10.1111/bre.12845
Pizzuto, J., Keeler, J., Skalak, K., & Karwan, D. (2017). Storage filters upland suspended sediment signals delivered from watersheds. *Geology*, *45*(2), 151–154. https://doi.org/10.1130/G38170.1
Roberge, L. (2025). loroberge/pub_Roberge_et_al_LandslideFluvialSedSignal_JGR-ES: Zenodo archive for JGR:ES submission (V1.0) [Software]. *Zenodo*. https://doi.org/10.5281/zenodo.17264139
Sharman, G. R., Sylvester, Z., & Covault, J. A. (2019). Conversion of tectonic and climatic forcings into records of sediment supply and provenance. *Scientific Reports*, *9*(1), 4115. https://doi.org/10.1038/s41598-019-39754-6
Shobe, C. M., Tucker, G. E., & Anderson, R. S. (2016). Hillslope-derived blocks retard river incision. *Geophysical Research Letters*, *43*(10), 5070–5078. https://doi.org/10.1002/2016GL069262
Shobe, C. M., Tucker, G. E., & Barnhart, K. R. (2017). The SPACE 1.0 model: A landlab component for 2-D calculation of sediment transport, bedrock erosion, and landscape evolution. *Geoscientific Model Development*, *10*(12), 4577–4604. https://doi.org/10.5194/gmd-10-4577-2017
Sifuentes, C., Martin, H. K., Straub, K. M., Hajek, E. A., & Edmonds, D. A. (2025). Floodplain topography and avulsion pathfinding control stratigraphic architecture in a numerical model of a fluvial fan. *Journal of Sedimentary Research*, *95*(1), 209–222. https://doi.org/10.2110/jsr.2024.045
Snyder, N. P., Whipple, K. X., Tucker, G. E., & Merritts, D. J. (2003). Importance of a stochastic distribution of floods and erosion thresholds in the bedrock river incision problem. *Journal of Geophysical Research*, *108*(B2). https://doi.org/10.1029/2001JB001655
Straub, K. M., Duller, R. A., Foreman, B. Z., & Hajek, E. A. (2020). Buffered, incomplete, and shredded: The challenges of reading an imperfect stratigraphic record. *Journal of Geophysical Research: Earth Surface*, *125*(3), e2019JF005079. https://doi.org/10.1029/2019JF005079
Thaler, E. A., & Covington, M. D. (2016). The influence of sandstone caprock material on bedrock channel steepness within a tectonically passive setting: Buffalo national river basin, Arkansas, USA. *Journal of Geophysical Research: Earth Surface*, *121*(9), 1635–1650. https://doi.org/10.1002/2015JF003771
Thomson, D. J. (1982). Spectrum estimation and harmonic analysis. *Proceedings of the IEEE*, *70*(9), 1055–1096. https://doi.org/10.1109/PROC.1982.12433
Tucker, G. E. (2004). Drainage basin sensitivity to tectonic and climatic forcing: Implications of a stochastic model for the role of entrainment and erosion thresholds. *Earth Surface Processes and Landforms*, *29*(2), 185–205. https://doi.org/10.1002/esp.1020
Tucker, G. E., & Bras, R. L. (1998). Hillslope processes, drainage density, and landscape morphology. *Water Resources Research*, *34*(10), 2751–2764. https://doi.org/10.1029/98WR01474
Weedon, G. P. (2003). *Time series analysis and cyclostratigraphy: Examining stratigraphic records of environmental cycles*. Cambridge University Press.
Wobus, C., Whipple, K. X., Kirby, E., Snyder, N., Johnson, J., Spyropolou, K., et al. (2006). Tectonics from topography: Procedures, promise, and pitfalls. In S. D. Willett, N. Hovius, M. T. Brandon, & D. M. Fisher (Eds.), *Tectonics, climate, and landscape evolution*. Geological Society of America. https://doi.org/10.1130/2006.239804
Yang, D., Huang, Y., Li, X., Gao, J., Yin, S., & Wang, C. (2024). Grain-size component dependent storage threshold of orbital cycles in alluvial stratigraphy caused by autogenic dynamics. *Sedimentology*, *71*(5), 1686–1704. https://doi.org/10.1111/sed.13187
Zhang, L., Parker, G., Stark, C. P., Inoue, T., Viparelli, E., Fu, X., & Izumi, N. (2015). Macro-roughness model of bedrock–alluvial river morphodynamics. *Earth Surface Dynamics*, *3*(1), 113–138. https://doi.org/10.5194/esurf-3-113-2015
Zinger, J. A., Rhoads, B. L., & Best, J. L. (2011). Extreme sediment pulses generated by Bend cutoffs along a large meandering river. *Nature Geoscience*, *4*(10), 675–678. https://doi.org/10.1038/ngeo1260

References From the Supporting Information

Ahnert, F. (1976). Brief Description of a Comprehensive Three-Dimensional Process-Response Model of Landform Development. Zeitschrift Für Geomorfologie. *Supplementband*, *25*, 29–49.
Carretier, S., Martinod, P., Reich, M., & Godderis, Y. (2016). Modelling sediment clasts transport during landscape evolution. *Earth Surface Dynamics*, *4*(1), 237–251. https://doi.org/10.5194/esurf-4-237-2016
Culmann, K. (1875). *Die graphische Statik. Zurich: Verlag von Meyer und Zeller*. Zurich.
Densmore, A. L., Ellis, M. A., & Anderson, R. S. (1998). Landsliding and the evolution of normal-fault-bounded Mountains. *Journal of Geophysical Research*, *103*(B7), 15203–15219. https://doi.org/10.1029/98JB00510
Johnstone, S. A., & Hilley, G. E. (2015). Lithologic control on the form of soil-mantled hillslopes. *Geology*, *43*(1), 83–86. https://doi.org/10.1130/G36052.1